

Article

Synthesis of Plasma-Reduced Graphene Oxide/Lithium Titanate Oxide Composite and Its Application as Lithium-Ion Capacitor Anode Material

Chan-Gyo Kim ^{1,†}, Suk Jekal ^{1,†}, Zambaga Otgonbayar ¹, Jiwon Kim ¹, Yoon-Ho Ra ¹, Jungchul Noh ² ,
Won-Chun Oh ³  and Chang-Min Yoon ^{1,*} 

¹ Department of Chemical and Biological Engineering, Hanbat National University, Daejeon 34158, Republic of Korea

² McKetta Department of Chemical Engineering and Texas Material Institute, The University of Texas at Austin, Austin, TX 78712, USA

³ Department of Advanced Materials Science and Engineering, Hanseo University, Seosan-si 31962, Republic of Korea

* Correspondence: cmyoon4321@hanbat.ac.kr; Tel.: +82-42-821-1528; Fax: +82-42-821-1593

† These authors contributed equally to this work.

Abstract: A plasma-reduced graphene oxide/lithium titanate oxide (PrGO/LTO) composite is prepared as an anode material to enhance the performance of lithium-ion capacitors (LICs). The PrGO/LTO composite is synthesized by mixing graphene oxide (GO) and LTO, followed by a series of freeze-drying and plasma-treatment processes. PrGO forms a porous three-dimensional (3D) structure with a large surface area, effectively preventing the restacking of PrGO while covering LTO. The GO/LTO mixing ratio is controlled to optimize the final structure for LIC applications. In lithium-ion half-cell assembly, the PrGO/LTO-based anode with an 80% mixing ratio exhibits the highest specific capacity of 73.0 mAh g⁻¹ at 20 °C. This is attributed to the optimized ratio for achieving high energy density from LTO and high power density from PrGO. In a LIC full-cell comprising PrGO/LTO as the anode and activated carbon as the cathode, the energy and power densities at 1 A g⁻¹ are 40.3 Wh kg⁻¹ and 2000 W kg⁻¹, respectively, with a specific capacitance of 36.3 F g⁻¹ and capacitance retention of 94.1% after 2000 cycles. Its outstanding performance, obtained from incorporating 3D-structured PrGO with LTO at an optimized ratio, lowers the cell resistance and provides efficient lithium-ion diffusion pathways.

Keywords: plasma-reduced graphene oxide; freeze-drying; lithium titanate oxide; lithium-ion capacitor



Citation: Kim, C.-G.; Jekal, S.; Otgonbayar, Z.; Kim, J.; Ra, Y.-H.; Noh, J.; Oh, W.-C.; Yoon, C.-M. Synthesis of Plasma-Reduced Graphene Oxide/Lithium Titanate Oxide Composite and Its Application as Lithium-Ion Capacitor Anode Material. *Batteries* **2024**, *10*, 311. <https://doi.org/10.3390/batteries10090311>

Academic Editors: Carmen Lăzău and Cornelia Bandas

Received: 13 August 2024

Revised: 27 August 2024

Accepted: 29 August 2024

Published: 31 August 2024



Copyright: © 2024 by the authors. Licensee MDPI, Basel, Switzerland. This article is an open access article distributed under the terms and conditions of the Creative Commons Attribution (CC BY) license (<https://creativecommons.org/licenses/by/4.0/>).

1. Introduction

As the demand for energy increases, high-energy-density and high-performance energy storage devices, such as lithium-ion batteries and electrochemical capacitors (ECs), have begun to receive wide attention [1,2]. ECs are widely used in industrial applications, including electric vehicles, mobile devices, uninterruptible power supplies (UPSs), and renewable energy systems, owing to their advantageous characteristics of long-term cycling, rapid charge/discharge, and high power density [3–6]. Among the various types of ECs, electric double-layer capacitors (EDLCs) store electric charge through the physical absorption/desorption of ions using carbon-based active materials to achieve high power density [7]. However, conventional EDLCs have limitations as high-energy storage devices because of their low energy density and narrow operating voltage range. To overcome these drawbacks, lithium-ion capacitors (LICs) have been developed as advanced electrochemical energy-storage systems. LICs combine high-energy-density lithium-ion battery anode materials with high-power-density EDLC cathode materials to bridge the

gap between lithium-ion batteries and ECs [8]. This hybrid approach enables LICs to provide fast charge/discharge capabilities, extended cycle life, and improved energy storage capacity [9,10].

The selection of anode materials is crucial for determining the electrochemical performance and stability of LICs. Graphite has been widely used as an anode material in LICs because of its ability to efficiently intercalate lithium ions. However, the use of graphite as an anode material has drawbacks, such as volumetric changes during charging/discharging and the formation of lithium dendrites [11,12]. To resolve these issues, lithium titanate oxide (LTO, $\text{Li}_4\text{Ti}_5\text{O}_{12}$) has emerged as an alternative anode material owing to its zero-strain property and operation at a high voltage of 1.55 V, which prevents the formation of lithium dendrites [13,14]. Despite these advantages, LTO as an anode has intrinsically low electrical conductivity, which limits its high-rate capability [15]. Previously reported articles have stated that adding carbon and its derivatives to LTO to prepare the LIC anode materials results in higher electrochemical properties, by resolving the drawbacks of low electrical conductivity and rate capability of pristine LTO [16–18]. Among carbon-based materials, reduced graphene oxide (rGO) can prevent the agglomeration of LTO owing to its flexible structure and large surface area. This leads to effectively increased lithium ions and fast interfacial kinetics, ensuring rapid charge and discharge cycles, resulting in high power densities and reduced internal resistance within the LIC [19–21]. In addition, rGO derived from a two-dimensional (2D) structured graphene oxide precursor can provide a suitable substrate to immobilize LTO nanoparticles.

However, 2D-structured GO sheets have drawbacks such as volumetric changes during charging/discharging, due to the van der Waals forces and π - π interactions that occur between interfaces of sheets, resulting in hindered Li^+ movement [22–24]. Forming a three-dimensional (3D) structure in GO is one of the strategies to prevent restacking and hindered Li^+ movement. In addition, the freeze-drying method is a more favorable and cost-effective method to fabricate the 3D-structured GO without inducing significant chemical changes in GO [25]. In detail, the freeze-drying method can immobilize the structures by removing solvents, like water, at relatively low temperatures ($-80\text{ }^\circ\text{C}$), generating a large number of pores in the 3D structure. The formation of the 3D structure permits the immobilization of other nanomaterials, including LTO, resulting in improved electron movement [26–28]. Incorporating LTO with a 3D-structured GO can result in better ion transfer when applied to electrodes for energy storage systems.

For synthesizing rGO, various methods including hydrothermal treatment, calcination, and plasma-induced photothermal reduction, have been used and provide a high degree of reduction [29–32]. Among these methods, plasma-induced photothermal reduction is more advantageous due to its simple operation and high plasma power, which avoids dissolving materials in acid and preserves the porous 3D structure [33]. This method generates high-energy electrons and reactive species, enhancing reduction efficiency through localized heating and rapid electron transfer, thereby maintaining structural integrity while improving electrical conductivity and surface area [34–36]. In addition, employing the freeze-drying method with plasma treatment can provide reduced GO with a large surface area, which may enhance electrochemical performance by providing rapid charge dynamics and lithium-ion transport pathways when incorporated into LTO as an LIC anode material [37].

In this study, a plasma-reduced graphene oxide/lithium titanate oxide (PrGO/LTO) composite was successfully synthesized via a series of freeze-drying and plasma-treatment processes and used as an LIC anode material. This is the first study to employ 3D-structured PrGO synthesized by freeze-drying followed by plasma treatment to create a framework for the immobilization of LTO and to improve its electrochemical performance at high charge/discharge rates. The amount of LTO added to the GO solution was controlled within the range of 60–90% to investigate the optimal ratio for use as an LIC anode (referred to as PrGO/LTO#amount%). The weight ratios of LTO to GO for the final PrGO/LTO60, PrGO/LTO70, PrGO/LTO80, PrGO/LTO90 materials were set to be 6:4, 7:3, 8:2, and 9:1, re-

spectively. For the half-cell tests, the PrGO/LTO80-based cell exhibited the highest specific capacity of 73.0 mAh g^{-1} at 20 °C. The high performance of the PrGO/LTO80-based cell was attributed to its balanced incorporation ratio, which provided high energy and power densities at high current rates (C-rates). In the LIC full-cell assembly, PrGO/LTO80 and activated carbon (AC) were employed as the anode and cathode materials, respectively, with retention rates of 94.1% even after 2000 cycles. This suggests that the PrGO/LTO80 composite is a promising anode material for LIC applications. The remarkable electrochemical performance of the PrGO/LTO composite is due to the enhanced lithium-ion diffusion pathways formed by the 3D-structured material with a large surface area, confirming its potential as an effective electrode material for LICs.

2. Materials and Methods

2.1. Materials

Lithium titanate oxide (LTO, $\text{Li}_4\text{Ti}_5\text{O}_{12}$, 99.0%) and lithium hexafluorophosphate (LiPF_6) were purchased from Tokyo Chemical Industry (Tokyo, Japan). Graphite (200 mesh, $\leq 74 \mu\text{m}$), ethylene carbonate (EC), ethyl methyl carbonate (EMC), 1-methyl-2-pyrrolidinone (NMP), carbon black, and polyvinylidene fluoride (PVDF, $M_w = 534,000$) were acquired from Merck KGaA (Darmstadt, Germany). Sulfuric acid (H_2SO_4 , 99.5%), hydrogen chloride (HCl, 35.0%), sodium nitrate (NaNO_3 , 99.0%), and potassium manganate (KMnO_4 , 99.3%) were obtained from Samchun Chemical Co. (Seoul, Republic of Korea). All chemical reagents and materials were used without further treatment. Activated carbon (AC, diameter: 0.85–2.40 mm, specific surface area: $1000 \text{ m}^2 \text{ g}^{-1}$) was purchased from Kuraray Co., Ltd. (Tokyo, Japan).

2.2. Preparation of Graphene Oxide

Graphene oxide (GO) was prepared using a modified Hummers' method, as previously described in the literature. Prior to using Hummers' method, a ball-milling process was conducted on graphite for 48 h using zirconium oxide balls (1, 2, and 5 mm) to reduce the size of the graphite. NaNO_3 (0.5 g) and H_2SO_4 (20 mL) were mixed under stirring in an ice bath. As-milled graphite powder (1.0 g) was then added to the solution and vigorously stirred for 30 min. Subsequently, KMnO_4 (3.0 g) was slowly added to the solution for 30 min. The oxidation reaction was conducted at 35 °C to form a viscous slurry. Deionized (DI) water (178 mL) was then slowly added to the slurry, followed by the dropwise addition of H_2O_2 (2.5 mL). The resulting brownish GO solution was washed three times using a 1.0 M HCl aqueous solution, followed by multiple rinses with DI water until the pH of the solution reached 7.0. The resulting GO solution was centrifuged (9500 rpm) for 20 min to remove residues.

2.3. Preparation of Plasma-Reduced GO/LTO Composite (PrGO/LTO)

As-prepared GO powder (0.250 g) was dispersed in DI water and vigorously stirred for 30 min. LTO was ball-milled for 48 h using the zirconium oxide balls (1, 2, and 5 mm), and added to the GO solution. Subsequently, as-milled LTO powder (0.375, 0.583, 1.000, 2.250 g) was added to the GO solution, and stirred for additional 2 h (referred to as GO/LTO60, GO/LTO70, GO/LTO80, and GO/LTO90). The resulting GO/LTO solution was then frozen using liquid nitrogen, and freeze-dried for 48 h using a freeze-drying machine (TFD 8501, Ilshin Bio Base, Seoul, Republic of Korea). The freeze-dried GO/LTO was kept in a vacuum oven to remove moisture. The GO/LTO was treated under atmospheric plasma conditions using commercial plasma equipment (MyPL-100P, APP Co., Ltd., Hwaseong, Republic of Korea) to produce the plasma-reduced GO/LTO composite (PrGO/LTO). A plasma power of 200 W was applied with oxygen (25 sccm) and argon (4.5 L min^{-1}) to produce the plasma curtain by radio frequency (13.56 MHz). The freeze-dried GO/LTO was placed 1.0 cm vertically from the tube and exposed to the curtain for 30 s. The PrGO/LTO material was obtained and kept in vacuum oven overnight.

2.4. Characterization

The morphologies of LTO, GO, GO/LTO, and PrGO/LTO were analyzed using field-emission scanning electron microscopy (FE-SEM, S-4800, Hitachi, Tokyo, Japan). Fourier-transform infrared (FT-IR, Nicolet iS10, Thermo Fisher Scientific, Waltham, MA, USA) and Raman spectroscopy (QE Pro, Ocean Optics Inc., Largo, FL, USA) were used to determine the molecular structures of the materials. The crystal structures were obtained by X-ray diffraction (XRD, D8 Advance, Bruker Co., Billerica, MA, USA). X-ray photoelectron spectroscopy (XPS, K-alpha, Thermo Fisher Scientific, Waltham, MA, USA) was employed to examine the chemical states of the materials. The Brunauer–Emmett–Teller (BET) surface areas and Barrett–Joyner–Halenda (BJH) pore distributions of the materials were derived from N₂-sorption curves. (TriStar II 3020, Micromeritics, Norcross, GA, USA). The thermal stability of the LTO, GO, and PrGO/LTO samples was measured using thermogravimetric analysis (TGA2, Mettler Toledo GmbH, Columbus, OH, USA).

2.5. Electrochemical Analysis

The electrochemical performances of PrGO/LTO and pristine LTO half-cells, as well as AC//LTO and AC//PrGO/LTO LIC full-cells were measured using 2032 coin-type cells. For the half-cell measurement, lithium metal was used as both counter and reference electrodes. To prepare the anode, conductive additive (carbon black) and binder material (PVDF) were first mixed using a mortar and pestle, and dispersed in NMP solvent to achieve homogeneity. After adding the active material (PrGO/LTO and LTO), the resulting slurry was shuffled using a paste mixer (PDM-300, DAEHWATECH, Gyeonggi-do, Republic of Korea) with 800 rpm rotation and 750 rpm revolution for 2 h. The mass ratio of the active material, conductive additive, and binder material in NMP was set to 8:1:1. The resultant slurry was pasted on the copper foil (12 μm) using a doctor blade, achieving a uniform coating with a thickness of ca. 150 μm. After the coating process, the electrode was dried, and circular samples with a diameter of 14 mm were punched out for electrochemical testing. The mass loading of the active material was 7.6 mg cm⁻². As an electrolyte, a 1.0 M LiPF₆ solution in ethylene carbonate and ethyl methyl carbonate (EC/EMC, 3:7 v/v) was used. The cathode for the LIC full-cell was prepared using a similar experimental procedure to that of the anode, except activated carbon (AC) was used as the active material and aluminum foil as the current collector. All cell assemblies were conducted in a glove box (MOtek, Daejeon, Republic of Korea) purged with high-purity argon (99.9995%).

The galvanostatic charge/discharge (GCD) performance of the cells was characterized using multi-channel battery testing instruments (WBCS 3000, WonATech, Seoul, Republic of Korea). For half-cells, the potential ranges of the anode and the cathode were selected to be 1.0–2.5 V and 3.0–4.3 V vs. Li/Li⁺, respectively. For LIC full-cells, the GCD test was conducted within a potential range of 1.0–3.0 V. The specific capacitance of the cells was determined from their GCD curves using the following equation [38]:

$$C_s = \frac{q}{\Delta V \times m} = \frac{1}{\Delta V \times m} \int_{t_0}^t i dt \text{ (from GCD curves)} \quad (1)$$

where C_s is the specific capacitance (F g⁻¹), q is the total charge, ΔV is the potential range (V), m is the mass of the active material (g), i is the current (A), and t is the discharge time (s). The energy density (E , Wh kg⁻¹) and power density (P , W kg⁻¹) values of the LIC full-cell were calculated using the following equations [39]:

$$E = \frac{1}{2} \times (V_{\max}^2 - V_{\min}^2) \times C_s \times \frac{1000}{3600} \quad (2)$$

$$P = \frac{E}{\Delta t} \times \frac{3600}{1000} \quad (3)$$

where V_{\max} and V_{\min} are the initial and final potentials of the discharging process (V). The electrochemical impedance spectroscopy (EIS) analysis of the cells was conducted using

an electrochemical workstation (Zive SP1, WonATech, Seoul, Republic of Korea) across a frequency range of 100 kHz to 10 mHz with a 10 mV AC voltage.

3. Results and Discussion

3.1. Fabrication of PrGO/LTO Composite

Figure 1 shows a schematic overview of the preparation process for the PrGO/LTO composite. First, GO was synthesized via a modified Hummers' method, assisted by ball milling for size control [40]. The pH of the resulting GO was adjusted to 7.0 by washing with HCl, followed by rinsing with DI water, to prevent side reactions with LTO in acidic conditions [41,42]. The prepared GO was mixed with LTO in DI water and freeze-dried to synthesize the GO/LTO composite. To determine the optimal concentration that provides the greatest improvement in electrochemical performance when applied to the LIC anode, a GO/LTO solution was prepared by adjusting the amount of LTO to 60–90% of the amount of GO. During freeze-drying, the water content in the GO was removed to form brown, sponge-like GO sheets that covered the surface of the LTO. GO/LTO was then reduced by atmospheric plasma treatment under Ar and O₂ gases, generating plasma through low-frequency radio waves within the tube. The high-energy electrons and ions generated from the plasma collided with the oxygen-containing groups on the surface of GO/LTO, converting GO to PrGO, whereas LTO remained unchanged during the process, resulting in the formation of a black PrGO/LTO composite.

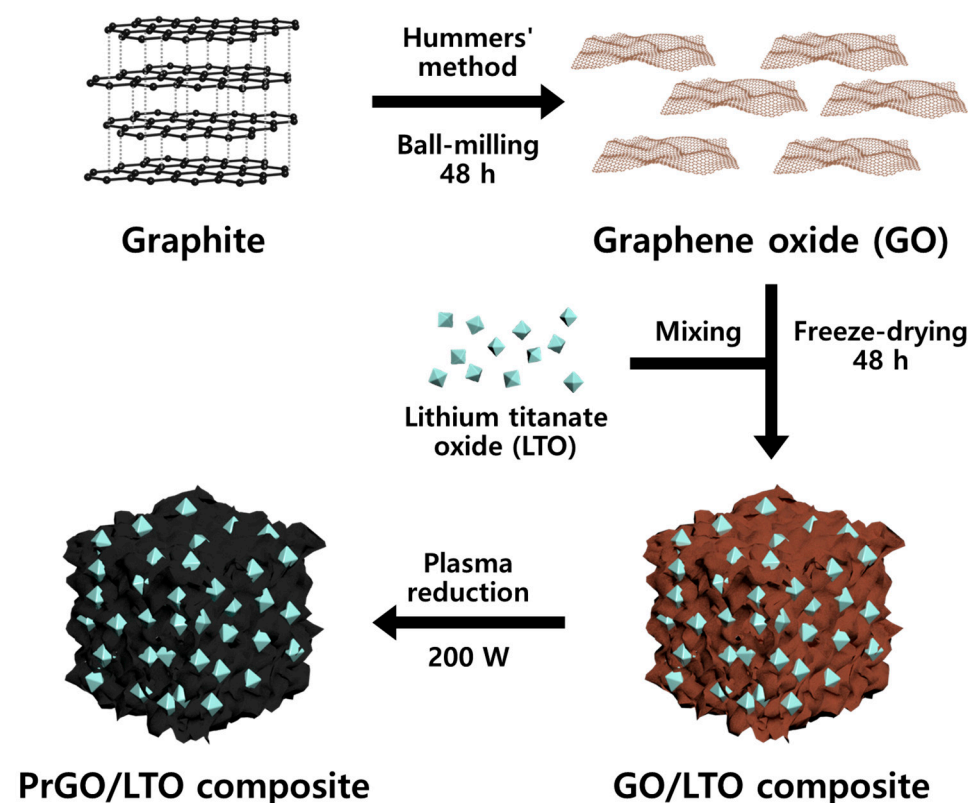


Figure 1. Schematic illustration of the preparation process of the plasma-reduced graphene oxide/lithium titanate oxide (PrGO/LTO) composite.

The structural and surface properties of pristine LTO, GO, GO/LTO, and PrGO/LTO were investigated using FE-SEM (Figure 2). For pristine LTO, spherical structures with diameters ranging from 300 to 500 nm were observed [43,44]. Freeze-dried GO exhibits a 3D structure formed by the random stacking of GO sheets [45]. In the case of GO/LTO, the LTO particles were successfully embedded within the 3D-structured GO matrix, confirming the effectiveness of the freeze-drying method in achieving structural advantages. However, distinct structural and surface properties were observed for PrGO/LTO. A large number of

mesopores are present in PrGO/LTO, with cracked pores marked by yellow dashed circles in the high-magnification scanning electron microscopy (SEM) images. In contrast, pores were not observed in either GO or GO/LTO, indicating the impact of plasma treatment in inducing porous structures, which is beneficial for electrochemical performance. SEM images of 60%, 70%, and 90% GO/LTO and PrGO/LTO are shown in Figure S1. In the case of PrGO/LTO90, fewer pores were observed owing to the larger amount of LTO. The analysis results demonstrate the critical role of plasma treatment in enhancing the structural properties of the composite, which directly contributes to its superior electrochemical performance. The formation of mesopores in PrGO/LTO not only increased the surface area but also provided additional active sites for lithium-ion adsorption, thereby improving ion transport and overall electrochemical activity. This study emphasizes synthesis methods for developing advanced materials for energy storage applications. The PrGO/LTO composite, with its unique structural features and enhanced performance, is a promising candidate for future high-performance LICs.

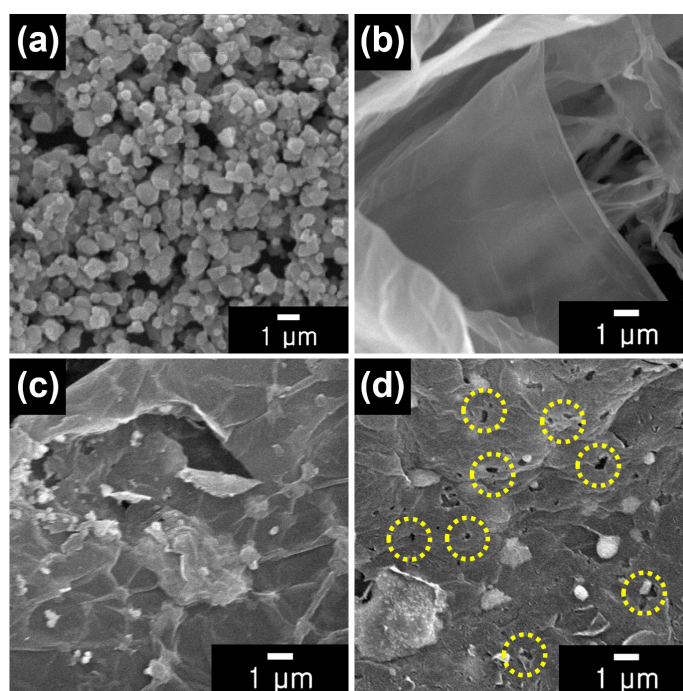


Figure 2. Field-emission scanning electron microscopy (FE-SEM) micrographs of (a) pristine LTO, (b) GO, (c) GO/LTO80, and (d) PrGO/LTO80.

FT-IR analysis was performed to characterize the presence of functional groups in pristine LTO, GO, GO/LTO80, and PrGO/LTO80 (Figure 3a). Pristine LTO showed a characteristic peak at 1114 cm^{-1} , and Li_2CO_3 peaks appeared at 1444 and 1493 cm^{-1} , respectively [46]. The spectrum of GO confirmed the successful oxidation of graphite, showing characteristic peaks at 1053 , 1621 , 1726 , and 3350 cm^{-1} , corresponding to the C–O, C=C, and C=O stretching of the carboxyl group and the O–H peak, respectively [47]. The spectrum of GO/LTO exhibited decreased intensity compared to that of GO owing to its mixing with LTO, which suggests successful integration of the two materials. After the reduction of GO/LTO80, the peaks of PrGO/LTO80 were diminished, which can be attributed to the characteristic limitation of FT-IR analysis in accurately measuring black and dark-gray materials. Nevertheless, the reduction process was indirectly confirmed by the changes observed in the spectrum, indicating the successful reduction of GO to PrGO. Raman spectroscopy was conducted to further analyze the structures of the materials, as shown in Figure 3b. For pristine LTO, an intense peak occurred at 680 cm^{-1} , corresponding to the vibrations of the Ti–O bonds in octahedral TiO_6 [48]. Additionally, the peaks at 429 and 353 cm^{-1} were attributed to the stretching and bending vibrations of the Li–O bonds

in polyhedral LiO_4 and LiO_6 , respectively [49]. LTO also exhibited a peak related to the bending vibration of the O–Ti–O bond at 231 cm^{-1} . Two characteristic peaks were detected for GO at 1354 and 1587 cm^{-1} , which correspond to the D-band and G-band of carbon materials, respectively [50]. The D-band indicates structural defects and disorder in carbon, whereas the G-band corresponds to the sp^2 graphitic carbon structure [51]. The spectrum of GO/LTO80 involves peaks related to both GO and LTO, with an increased D-band intensity to G-band intensity (I_D/I_G) ratio owing to the addition of LTO, which suggests an increase in structural disorder due to the incorporation of LTO. However, the I_D/I_G ratio decreased for PrGO/LTO80, indicating successful reduction by the plasma treatment, leading to a more ordered carbon structure and improved material properties. The effectiveness of the plasma reduction process in modifying the structural and surface properties of the composite materials was verified. The successful integration of LTO into the GO matrix and its subsequent reduction to PrGO/LTO80 demonstrated the potential of this composite for advanced electrochemical applications. Both FT-IR and Raman spectroscopy provide an overview of the molecular changes and structural enhancements achieved through the freeze-drying followed by plasma treatment employed in this study. Furthermore, the improvement in the structural integrity and electrochemical performance, particularly the increased conductivity and ion transport, has resulted in the development of high-performance anode materials for LICs.

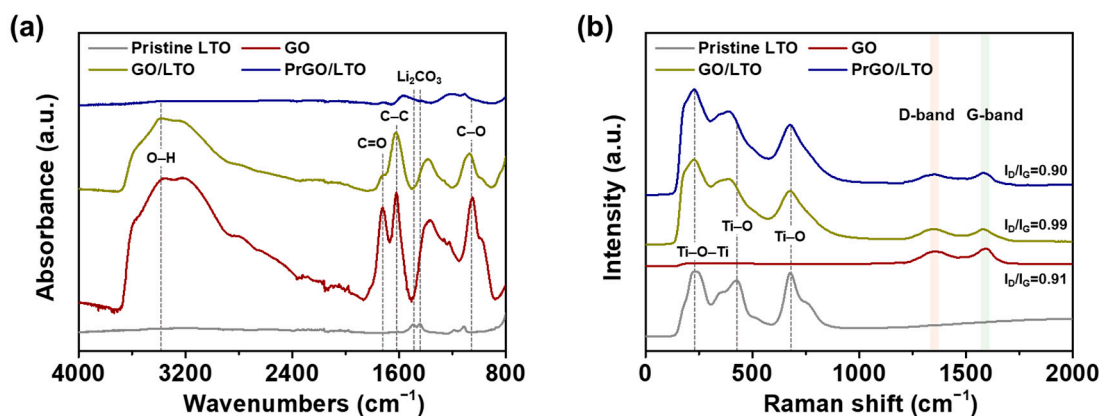


Figure 3. (a) Fourier transform infrared (FT-IR) and (b) Raman spectra of pristine LTO, GO, GO/LTO80, and PrGO/LTO80.

The XRD patterns were analyzed to investigate the crystallinity of pristine LTO, GO, GO/LTO80, and PrGO/LTO80 (Figure 4). The diffraction peaks of pristine LTO were detected at $2\theta = 18.4^\circ$, 35.6° , 43.3° , 47.5° , and 57.3° , corresponding to the (111), (311), (400), and (511) crystal planes of LTO, respectively (JCPDS No. 49-0207) [52]. In contrast, the XRD pattern of GO showed a broad peak around $2\theta = 11^\circ$, corresponding to the (001) plane of graphene oxide [53], which indicates a relatively low crystallinity typical of GO owing to the disordered stacking of oxidized graphene layers. The XRD pattern of GO/LTO80 exhibited the characteristic peaks of both LTO and GO, confirming the successful combination of these two materials in the composite. In the case of PrGO/LTO80, a broad diffraction peak appeared at 25.2° , corresponding to the (002) diffraction plane of graphitic carbon, which is indicative of the reduced form of graphene oxide [54]. Additionally, PrGO/LTO80 exhibited an extra peak at ca. 40.2° , suggesting the formation of a more graphitized structure after the plasma reduction process. Importantly, the LTO peaks observed for PrGO/LTO80 matched those of pristine LTO, indicating that the crystalline structure of LTO was well preserved during the freeze-drying and plasma treatment processes. This preservation of the crystalline integrity of LTO, along with the reduction of GO to PrGO, implies the

effectiveness of the synthesis methods employed. The interlayer spacing (d-spacing) values of GO/LTO80 and PrGO/LTO80 were calculated using Bragg's law [55]:

$$n\lambda = 2d\sin\theta, \quad (4)$$

where λ is the wavelength of the X-ray source. The d-spacing of GO/LTO80 and PrGO/LTO80 were calculated to be ca. 8.0 and 3.5 Å, respectively. The presence of oxidized graphene sheets in GO/LTO80 led to an increased interlayer spacing owing to the insertion of oxygen-containing groups between the graphene layers. This is evident from the broad diffraction peak of PrGO/LTO80, which indicates a modification of the graphitic structure as a result of the plasma treatment, suggesting the successful reduction of GO through the removal of oxygen-containing groups. Consequently, the XRD results confirmed not only the formation of PrGO but also the preservation of the crystal structure of LTO, even after freeze-drying followed by plasma treatment. In addition, the results demonstrated that the synthesis method effectively formed highly crystalline and electrochemically stable LTO with enhanced conductivity and surface properties of PrGO, making the PrGO/LTO composite a promising material for advanced electrochemical applications.

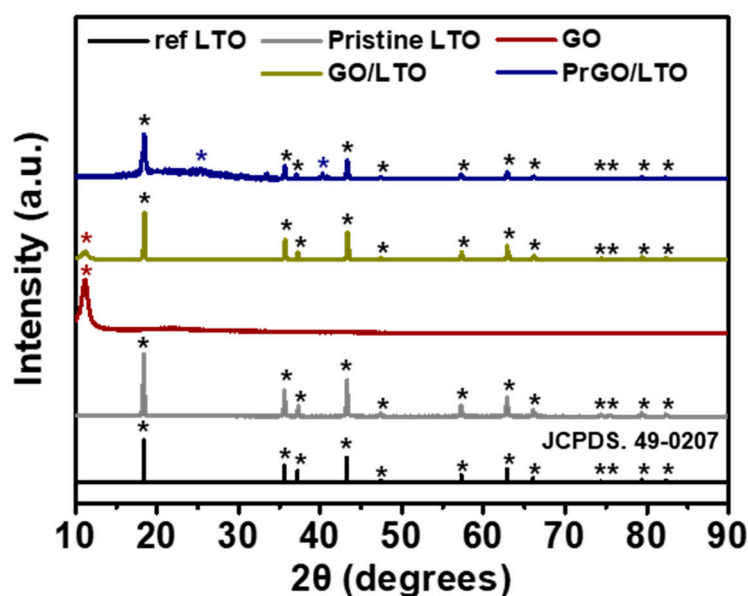


Figure 4. X-ray diffraction (XRD) patterns of pristine LTO, GO, GO/LTO80, and PrGO/LTO80.

The XRD patterns of LTO, GO/LTO, and PrGO/LTO samples were analyzed using Rietveld refinement, confirming that all samples crystallized in the spinel structure with the space group $Fd-3m$. The observed (Y_{obs}) and calculated (Y_{cal}) patterns are shown in the provided graphs for each sample (Figure 5). For LTO, the refinement indicated a good fit between the observed and calculated patterns, confirming the high crystallinity and phase purity ($R_{exp} = 31.2\%$, $R_{wp} = 17.7\%$, $R_p = 21.7\%$). The GO/LTO sample showed slight shifts in peak positions and intensities, suggesting successful composite formation ($R_{exp} = 63.1\%$, $R_{wp} = 6.76\%$, $R_p = 59.5\%$). The PrGO/LTO sample exhibited further modifications in the diffraction pattern, indicating interactions between PrGO and the LTO matrix, which may enhance the material properties ($R_{exp} = 8.3\%$, $R_{wp} = 21.4\%$, $R_p = 19.2\%$). The Bragg peaks are well-matched with the calculated patterns, demonstrating the accuracy of the refinement process (Table 1). These results are consistent with previously reported articles, which also reported the successful incorporation of graphene oxide and its derivatives into lithium titanate matrices, leading to improved structural and electrochemical properties [56–59].

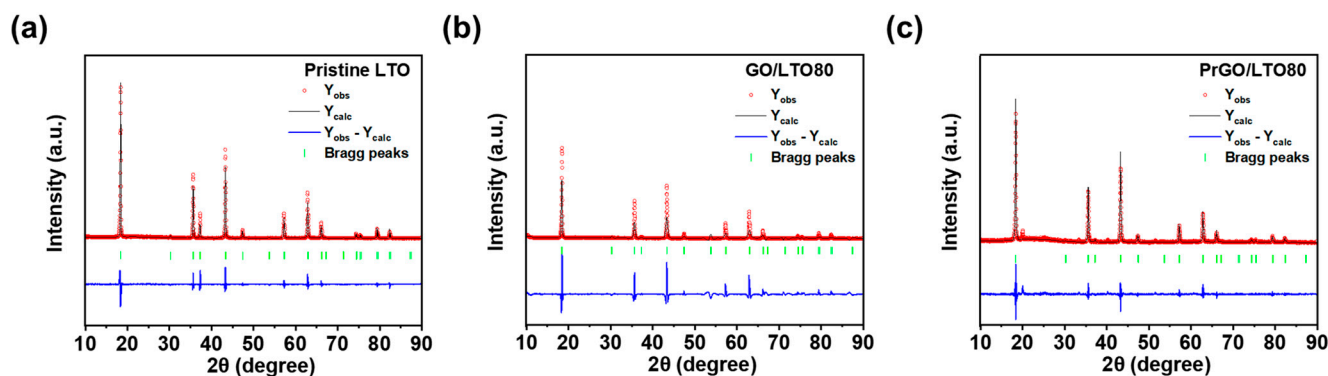


Figure 5. Rietveld refinement of XRD pattern of (a) pristine LTO, (b) GO/LTO80, and (c) PrGO/LTO80.

Table 1. Structural parameters of the LTO, GO/LTO80, and PrGO/LTO80 ^a.

Sample	Y_{obs}	Y_{cal}	Bragg R_{factor}	Vol (nm ³)	R_p (%)	R_{exp} (%)	R_{wp} (%)
LTO	3312.7	3312.5	2.6	583.6	21.7	31.2	17.7
GO/LTO80	30,127	2912.5	3.4	582.4	59.5	63.1	6.76
PrGO/LTO80	128.5	118.3	8.1	584.7	19.2	8.3	21.4

^a Structural parameters were obtained from Rietveld refinement of XRD.

XPS spectra were obtained to reveal the chemical states of LTO, GO, GO/LTO80, and PrGO/LTO80 (Figure S2). For pristine LTO, Li 1s, Ti 2p, C 1s, and O 1s peaks were observed. Specifically, LTO exhibited C 1s peaks at ca. 284.6 and 286.3 eV, corresponding to the C–C and C–O bonds typically found in carbon contamination, respectively (Figure 6). Additionally, high-resolution XPS spectra showed that two Ti 2p and one Li 1s characteristic peaks appeared at 457.2, 463.0, and 53.6 eV caused by the Ti⁴⁺ and Li⁺ valence state of LTO, respectively (Figure S3) [60,61]. The O 1s spectrum of LTO was deconvoluted into two peaks at ca. 531.4 and 529.6 eV, suggesting contamination and the Ti–O band (Figure S4) [62]. However, only the C 1s and O 1s peaks were observed for GO. In the C 1s spectra, high-intensity peaks corresponding to oxygen-containing (i.e., C–O and C=O) groups were observed at ca. 286.4 and 287.6 eV, respectively, along with the C–C peak at ca. 284.6 eV, indicating the oxidation of graphite [63]. Additionally, peaks associated with the C–O and C=O groups were observed for GO in the O 1s spectrum at 532.1 and 530.2 eV, respectively [64]. For GO/LTO80 and PrGO/LTO80, only the peak intensities of the Li 1s and Ti 2p spectra decreased compared to those of pristine LTO, indicating that there were no chemical changes after plasma treatment. In the C 1s spectrum, GO/LTO exhibited the same peaks as those of GO; however, the peak intensities were lower than those of GO owing to the mixing of LTO with GO. In the case of PrGO/LTO80, the intensities of the C 1s peaks for the oxygen-containing groups were significantly decreased compared to those of GO, whereas the intensity of the C–C peak increased, verifying the successful transformation of the oxygen-containing groups into carbon-based groups and indicating a higher degree of graphitization of the sp² carbon network. Besides the C 1s peaks, the intensity of the C=O peak in the O 1s spectrum was higher than that of the C–O peak, verifying successful reduction by plasma treatment. Consequently, the XPS spectra confirmed that both pristine LTO and GO exhibit characteristic peaks consistent with their expected chemical states. The GO/LTO80 and PrGO/LTO80 samples show modifications in peak intensities and shifts, indicative of minimal chemical changes post-plasma treatment for GO/LTO80 and significant reduction and increased graphitization for PrGO/LTO80.

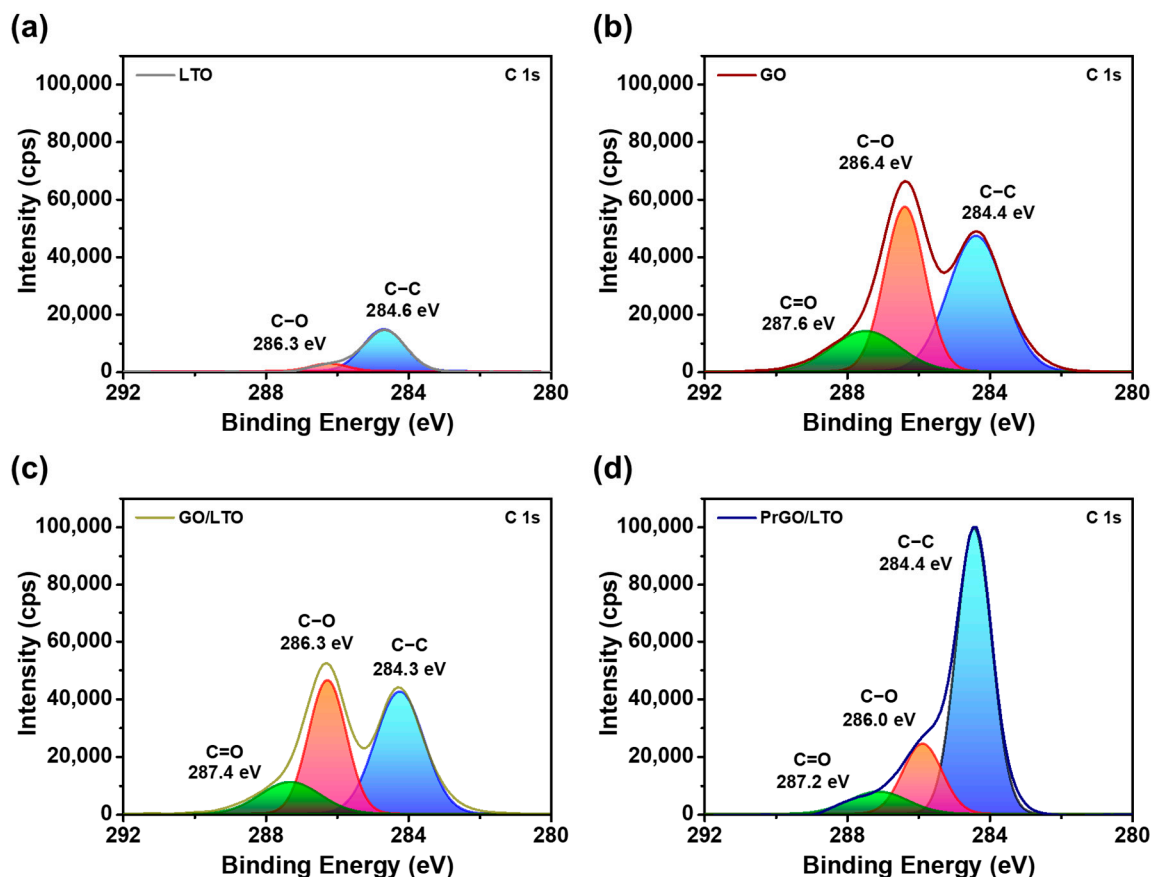


Figure 6. X-ray photoelectron spectroscopy (XPS) C 1s spectra of (a) pristine LTO, (b) GO, (c) GO/LTO80, and (d) PrGO/LTO80.

To evaluate the porous structures of pristine LTO, GO, GO/LTO, and PrGO/LTO, the BET surface area and BJH pore distributions were analyzed using N_2 -sorption isotherms (Figure 7). Pristine LTO exhibited typical type-II hysteresis curves, reflecting its nonporous characteristics [65]. Conversely, type-IV hysteresis curves were observed for GO, GO/LTO80, and PrGO/LTO80, indicating their porous nature [66]. This porosity was induced by the freeze-drying process, which preserved the interlayer spacing within the graphene-based materials. The specific surface areas and pore size distributions of pristine LTO, GO, GO/LTO, and PrGO/LTO are listed in Table S1. GO possessed a larger surface area of $19.3 \text{ m}^2 \text{ g}^{-1}$ compared to that of LTO ($5.4 \text{ m}^2 \text{ g}^{-1}$), attributed to oxygen-containing functional groups, such as carboxyl ($-\text{COOH}$), hydroxyl ($-\text{OH}$), and epoxy ($-\text{C}-\text{O}-\text{C}-$) groups, that prevent the restacking of GO sheets. After mixing LTO with GO in different ratios, the surface areas of GO/LTO60, GO/LTO70, GO/LTO80, and GO/LTO90 were distributed between those of LTO and GO, with values of 15.8 , 14.1 , 13.3 , and $12.8 \text{ m}^2 \text{ g}^{-1}$, respectively. These values verified the presence of LTO particles occupying the space between the GO sheets. The surface areas of PrGO/LTO60, PrGO/LTO70, PrGO/LTO80, and PrGO/LTO90 increased drastically compared with those of the corresponding GO/LTO composites, with values of 126.6 , 110.9 , 94.1 , and $72.8 \text{ m}^2 \text{ g}^{-1}$, respectively, along with the presence of a dominant pore size of ca. 3.9 – 4.1 nm . This increase was attributed to the effects of freeze-drying and plasma treatment, which induced the formation of numerous mesopores [67–69]. As the amount of LTO increased, the surface area decreased, confirming that the proportion of PrGO positively affected the porosity of the materials. Thus, BET and BJH analyses revealed that while pristine LTO remained nonporous, the incorporation of GO and subsequent plasma treatment in the GO/LTO and PrGO/LTO composites significantly enhanced their surface areas and porous structures. This increase

in the surface area and pore structure facilitates the improved electrochemical performance of the LIC electrodes.

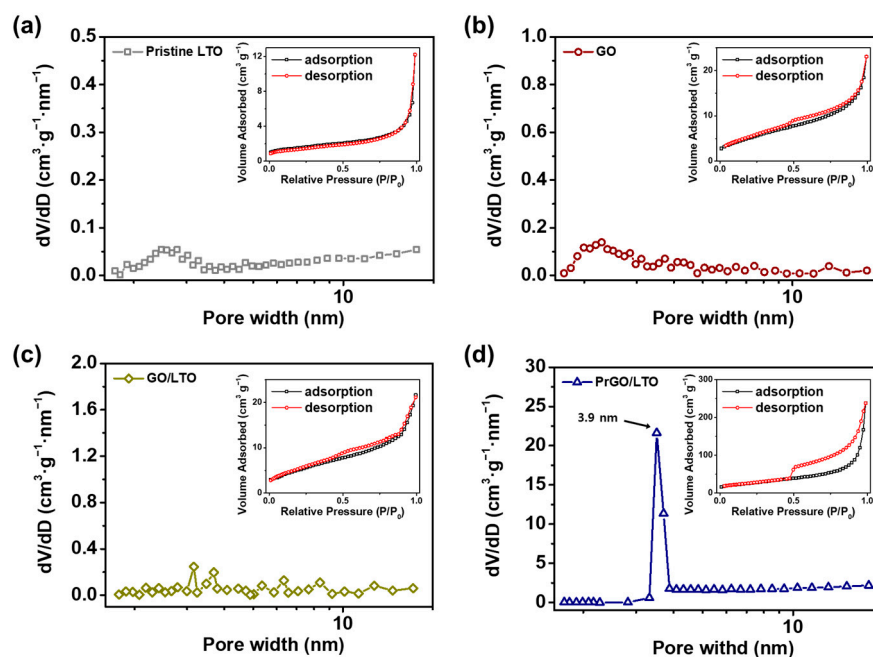


Figure 7. Barrett–Joyner–Halenda (BJH) pore size distribution curves of (a) pristine LTO, (b) GO, (c) GO/LTO80, and (d) PrGO/LTO80 (insets: corresponding N_2 adsorption/desorption curves).

Thermogravimetric analysis (TGA) was conducted to investigate the temperature-dependent characteristics of the LTO, GO, and PrGO/LTO samples under O_2 conditions within a temperature range of 30–750 °C. Figure 8 shows the TGA results for the samples. Pure LTO exhibited a slight weight loss at 100 °C, corresponding to the loss of adsorbed water. No other decomposition peaks were observed for pristine LTO, indicating its high thermal stability across the temperature range [70,71]. For the PrGO/LTO samples, three stages of decomposition were observed: below 100 °C, 150–380 °C, and 380–550 °C. The first decomposition peak is related to water vaporization. The subsequent peaks are associated with the decomposition of oxygen-containing functional groups and elimination of aromatic carbons ($-C=C-$) in GO [72–74]. The decomposition of PrGO/LTO varied with the GO loading amount, with the maximum decomposition peak at 468.7 °C for PrGO/LTO. As PrGO decreased, the decomposition peak intensity related to GO decreased, indicating increased stability at higher temperatures. LTO became the dominant factor for the thermal stability of the PrGO/LTO samples. In addition, the weight percentage of PrGO in the PrGO/LTO samples was calculated by subtracting the remaining weight of LTO from the PrGO/LTO samples. It was estimated that the measured weights were ca. 58.2%, 99.3%, 79.8%, 84.2%, 88.7%, and 91.3% for GO, LTO, PrGO/LTO60, PrGO/LTO70, PrGO/LTO80, and PrGO/LTO90, respectively. TGA results verified that PrGO/LTO with optimum GO loading can withstand operational conditions without degradation, thus ensuring consistent performance of the LIC.

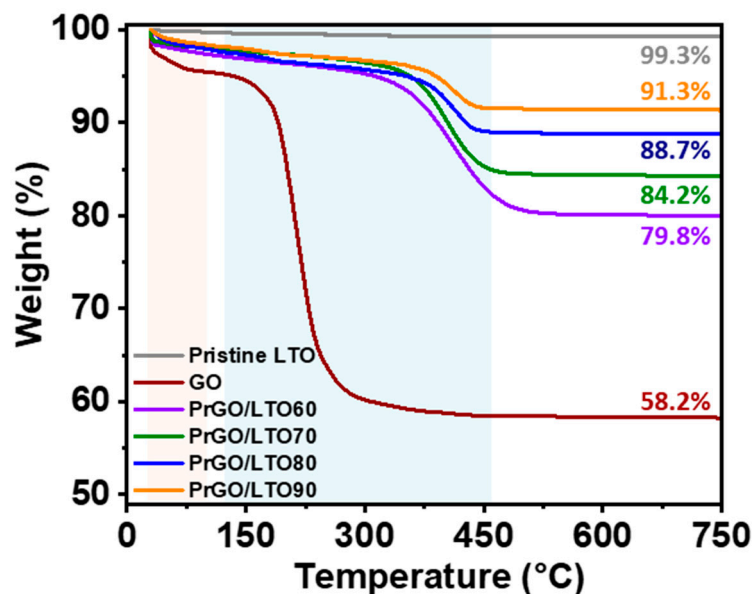


Figure 8. TGA analysis of pristine LTO, GO, PrGO/LTO60, PrGO/LTO70, PrGO/LTO80, and PrGO/LTO90.

3.2. Electrochemical Performance of PrGO/LTO-Based Electrodes

The electrochemical performance of the PrGO/LTO-based electrodes was evaluated using a half-cell assembly, where the PrGO/LTO composite served as the working electrode, lithium as the counter and reference electrodes, and 1.0 M LiPF₆ in a mixture of EC and EMC (3:7 *v/v*) as the electrolyte. To assess the electrochemical behavior, various tests such as charge/discharge, rate capability, and electrochemical impedance spectroscopy (EIS) were performed. The specific capacities of PrGO/LTO60-, PrGO/LTO70-, PrGO/LTO80-, and PrGO/LTO90-based electrodes were measured at different C-rates, ranging from 0.1 to 20.0 C within a voltage range of 1.0–2.5 V, as depicted in Figure 9a–e. For comparison, the capacities of the pristine LTO-based cells were also measured at the same C-rates (Figure S5). The discharge capacities of the LTO-based electrode at 0.1, 1.0, 2.0, 5.0, and 10.0 C were measured as ca. 151.7, 139.0, 128.2, 95.9, and 52.0 mAh g⁻¹. However, as the C-rate increased to 20 C, the discharge capacity of the pristine LTO-based electrode rapidly decreased, ultimately reaching 21.9 mAh g⁻¹. This significant drop in capacity can be attributed to the inherently low electrical conductivity of pristine LTO, which hinders efficient electron transport during high-rate charging and discharging. In addition, pristine LTO lacks the ability to facilitate the rapid movement of electrons without the aid of conductive carbon materials, leading to a substantial performance degradation at high C-rates. In contrast, all the PrGO/LTO-based electrodes exhibited higher discharge capacities at 20 C than the pristine LTO-based electrode. This improvement is primarily due to the presence of three-dimensional (3D)-structured PrGO, which provides a wide pathway for lithium-ion diffusion and enhances electrical conductivity during the charging/discharging processes. Among the different composites, the PrGO/LTO80-based electrode demonstrated the highest discharge capacity of 73.0 mAh g⁻¹ at 20 C, suggesting that an optimal amount of LTO is essential to maintain high capacity at elevated C-rates. The discharge capacities of the various PrGO/LTO-based electrodes are detailed in Table S2.

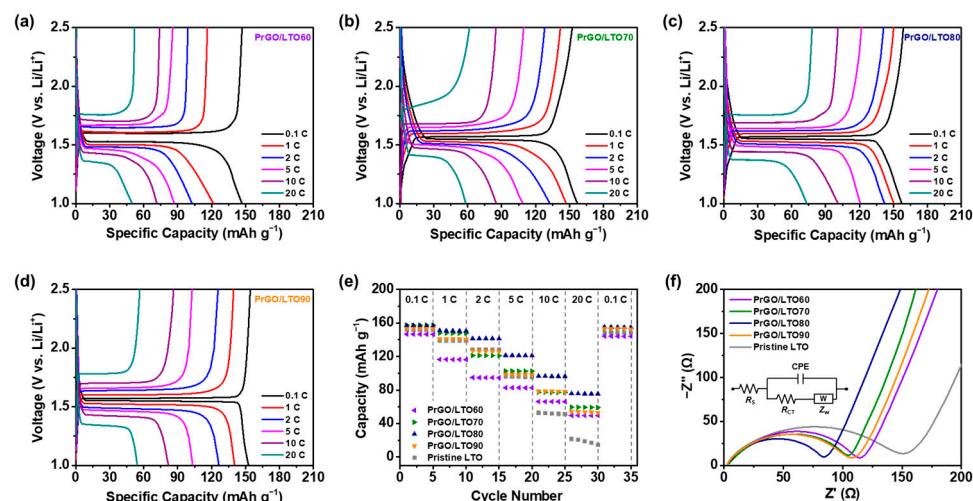


Figure 9. Galvanostatic charge/discharge (GCD) curves of (a) PrGO/LTO60-, (b) PrGO/LTO70-, (c) PrGO/LTO80-, and (d) PrGO/LTO90-based electrodes at different current rates (C-rates) from 0.1 to 20.0 C. (e) Rate capability from 0.1 to 20.0 C and (f) electrochemical impedance spectroscopy (EIS) curves for various PrGO/LTO- and pristine LTO-based electrodes.

To gain a deeper understanding of the contribution of PrGO to the electrochemical behavior of LTO, electrochemical impedance spectroscopy (EIS) analysis was conducted on various PrGO/LTO- and pristine LTO-based electrodes. Nyquist plots are presented in Figure 9f, with the inset showing the equivalent circuit used for fitting the EIS data. According to the literature, the circuit includes an equivalent series resistance (R_S), representing the ionic resistance in the electrolyte and the surface resistance of the electrodes; charge-transfer resistance (R_{CT}), reflecting the resistance of ion reactions at the electrode–electrolyte interface; a constant phase element (CPE) representing double-layer capacitance; and Warburg impedance (Z_W) associated with lithium-ion diffusion [75]. In the high-frequency region, a semicircle centered on the real axis was observed in all EIS curves, indicating capacitive behavior owing to CPE. The R_S values for the PrGO/LTO60-, PrGO/LTO70-, PrGO/LTO80-, PrGO/LTO90-, and pristine LTO-based electrodes were ca. 3.4, 3.2, 2.9, 3.1, and 3.5 Ω , respectively, while the R_{CT} values were around 120.2, 110.7, 85.8, 116.1, and 160.2 Ω , respectively. Notably, the R_S values across all electrodes were similar, suggesting that R_S is not directly influenced by the proportion of PrGO and LTO. However, the R_{CT} values varied with the mixing ratio, with the PrGO/LTO80-based electrode exhibiting the lowest R_{CT} value. This was attributed to the optimal mixing ratio, which facilitated rapid and efficient lithium-ion transfer. For the pristine LTO- and PrGO/LTO90-based electrodes, the absence or insufficient amount of PrGO resulted in low conductivity [76], whereas an excessive amount of PrGO reduced the amount of LTO available for lithium-ion supply, thereby reducing the performance [77]. In the low-frequency region, the Warburg impedance appeared as a straight line, indicating lithium-ion diffusion within the pristine LTO. The significant enhancement in the electrochemical performance, as observed in both EIS and other electrochemical measurements, is due to the synergistic effects of PrGO and LTO in the composite. The 3D porous structure of PrGO offers an extensive surface area and shortens the diffusion pathways for lithium ions, thereby improving the overall ion transport and electron mobility within the electrode. Moreover, the optimal PrGO/LTO ratio, particularly at 80%, ensures a balanced combination of the high electrical conductivity of PrGO and the sufficient lithium-ion storage capacity of LTO. This balance leads to reduced charge-transfer resistance, lower internal resistance, and enhanced rate capability, which collectively contribute to the superior electrochemical performance, long-term stability, and high capacity retention of the PrGO/LTO80-based electrodes.

Consequently, the electrochemical performance evaluations and impedance spectroscopy demonstrate that the PrGO/LTO composites, particularly with an optimal PrGO

content of 80%, significantly outperform pristine LTO electrodes by enhancing electrical conductivity, reducing charge-transfer resistance, and improving rate capability, thereby ensuring superior electrochemical performance, long-term stability, and high capacity retention.

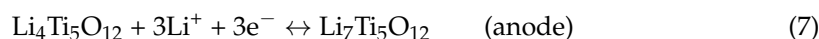
3.3. Electrochemical Performance of the AC//PrGO/LTO80 Full-Cell

The potential application of PrGO/LTO was evaluated in a LIC full-cell assembly, where PrGO/LTO was used as the anode and AC was used as the cathode. Prior to the assembly, the electrochemical performance of the AC-based electrode was evaluated, and the corresponding charge/discharge curves at different current densities, ranging from 0.05 to 2.00 A g⁻¹, are shown in Figure S5. These curves maintain a symmetric triangular shape with a slight IR drop, suggesting that AC is a suitable material for LIC cathodes with efficient capacitive behavior. The mass ratio of the cathode to anode material was balanced to maximize the energy density of the LIC according to the following equation [78]:

$$\frac{m^+}{m^-} = \frac{Q_{SP}^-}{Q_{SP}^+}, \quad (5)$$

where Q_{SP} is the specific capacity and m is the mass of the active material. From the capacity profiles of the half-cells, the typical capacity of the PrGO/LTO80 anode was selected as 121.4 mAh g⁻¹ at 5 C, whereas the specific capacity of the AC cathode was measured to be ca. 117.4 F g⁻¹ (42.4 mAh g⁻¹) at a current density of 0.05 A g⁻¹. Hence, the theoretical mass ratio was set to 1:2.5. Electrochemical measurements of the cells were conducted several times to ensure reproducibility of the energy balance. For comparison, an LIC full-cell using pristine LTO and AC was assembled (AC//LTO) using the same method as for the AC//PrGO/LTO80 full-cell.

The electrochemical performance of the assembled AC//LTO and AC//PrGO/LTO80 full-cells was evaluated using various analytical methods. First, galvanostatic charge/discharge (GCD) curves of the LIC cells were measured at different current densities ranging from 0.05 to 1.00 A g⁻¹, as shown in Figure 10a,b. In both cells, an asymmetric slope of the discharge curves was observed, indicating a difference in the energy storage mechanisms of the cathode and anode. Specifically, the charging/discharging of the AC//PrGO/LTO80 cell involved the insertion/extraction of lithium ions from PrGO/LTO80 and the interfacial adsorption/desorption of anions on the AC surface. The detailed reaction equations are as follows [79]:



The AC//LTO cell showed a higher IR drop compared to that of the AC//PrGO/LTO80 cell because of the higher resistance caused by the absence of a conductive material. The specific capacitance values of the AC//PrGO/LTO80 cell from GCD curves ranged from 65.1 to 43.8 F g⁻¹ at current densities of 0.05 to 1.00 A g⁻¹, whereas those of the AC//LTO cell ranged from 56.9 to 19.2 F g⁻¹. Notably, the AC//PrGO/LTO80 cell showed a higher rate capability (67.3%) than that of the AC//LTO cell (33.7%), confirming the effect of incorporating the conductive material into LTO. Figure 10c shows the specific capacitance values of the AC//PrGO/LTO80 and AC//LTO cells at different current densities, as determined by the GCD curves.

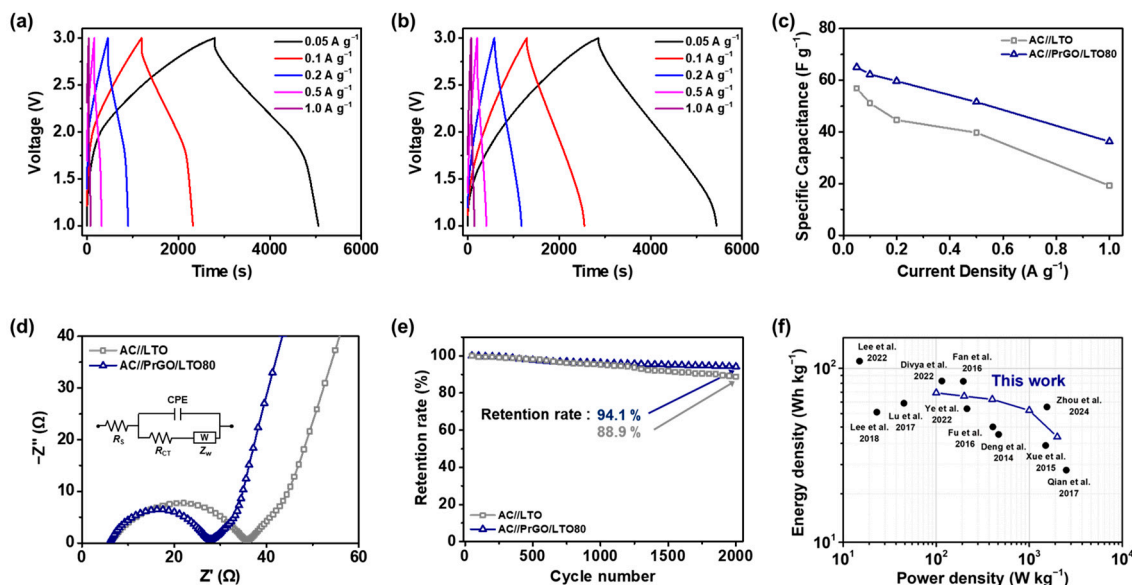


Figure 10. GCD curves of (a) AC//LTO and (b) AC//PrGO/LTO80 LIC full-cells at different current densities from 0.05 to 1.00 A g^{-1} . (c) Specific capacitances of the LIC cells calculated from the GCD curves. (d) EIS analysis and (e) cyclability test results of the cells. (f) Ragone plot of the AC//PrGO/LTO80 cells compared to other previously studied LIC cells. Reproduced by: Lu et al., 2017 [80], Fu et al., 2016 [81], Qian et al., 2017 [82], Deng et al., 2014 [83], Xue et al., 2015 [84], Lee et al., 2018 [85], Fan et al., 2016 [86], Ye et al., 2022 [87], Zhou et al., 2024 [88], Divya et al., 2022 [89], and Lee et al., 2022 [90].

The ion diffusion capabilities of the LICs were evaluated using EIS analysis, and the equivalent circuit diagram is shown in Figure 10d. The R_s and R_{ct} values for the AC//PrGO/LTO80 cell were 6.0 Ω and 22.1 Ω , respectively, which are lower than those of the AC//LTO cell (6.24 Ω and 35.9 Ω , respectively). Additionally, the cycle stability of the LIC cells was tested by performing charge/discharge cycles at a current density of 0.5 A g^{-1} for 2000 cycles (Figure 10e). The capacity retention of the AC//PrGO/LTO80 cell reached 94.1%, compared to 88.9% for the AC//LTO cell. The incorporation of the highly conductive PrGO material improved the ion transport capability and cycling performance by providing shorter diffusion pathways for lithium ions. The energy and power densities of the LIC cells were compared with those of other supercapacitors (Figure 10f) [80–90]. The LIC using the AC//PrGO/LTO80 cell showed superior power and energy densities compared to previously reported articles, including NGA/LTO [86], AC/CNT-chained LTO [87], AC/LTO [88], AC/pre-lithiated LTO [89], and Si/LTO [90]. The maximum energy density of the AC//PrGO/LTO80 cell was calculated to be 72.3 Wh kg^{-1} at a power density of 100 W kg^{-1} . In addition, the cell was capable of delivering a power density of 2000 W kg^{-1} while maintaining an energy density of 40.3 Wh kg^{-1} . The LIC cell assembled in this study demonstrated remarkable energy and power densities compared to those of other cells.

These results indicate that PrGO/LTO80 exhibits enhanced electrochemical performance compared to pristine LTO, which is attributed to the incorporation of PrGO, which provides a larger surface area and high electrical conductivity (Figure 10). Therefore, the assembled AC//PrGO/LTO80 LIC cell, with its high specific capacitance, energy density, and power density, shows significant potential as an anode material for advanced LIC. The enhanced electrochemical performance observed by EIS and other electrochemical analyses can be attributed to the unique structural and co-positional properties of the plasma-reduced graphene oxide/lithium titanate oxide (PrGO/LTO) composite. This synthesis method, combining freeze-drying and plasma reduction, resulted in a 3D porous structure that significantly improved lithium-ion diffusion and electron transport. This 3D

porous structure prevents the restacking of graphene oxide sheets, maintains a large surface area, and facilitates efficient ion transfer. Moreover, the plasma reduction process not only reduced GO but also introduced mesopores within PrGO, providing additional active sites for lithium-ion adsorption and enhancing the overall electrochemical activity. The synergistic integration of LTO into the conductive PrGO matrix optimized the performance of the composite by balancing the energy and power densities, particularly at 80% LTO composition. This optimal ratio improves the high energy-storage capacity of LTO, while benefiting from the superior conductivity and rapid electron transport capabilities of PrGO. Consequently, the composite exhibited reduced charge transfer resistance (R_{CT}), lower internal resistance, and improved rate capabilities, as evidenced by the EIS results. The correlation between these factors led to enhanced electrochemical kinetics, superior energy storage performance, and excellent long-term stability, making the PrGO/LTO composite a promising candidate for high-performance LICs.

The plausible mechanism for attaining high electrical conductivity and a shorter lithium-ion diffusion property by adding PrGO to pristine LTO is shown in Figure 11.

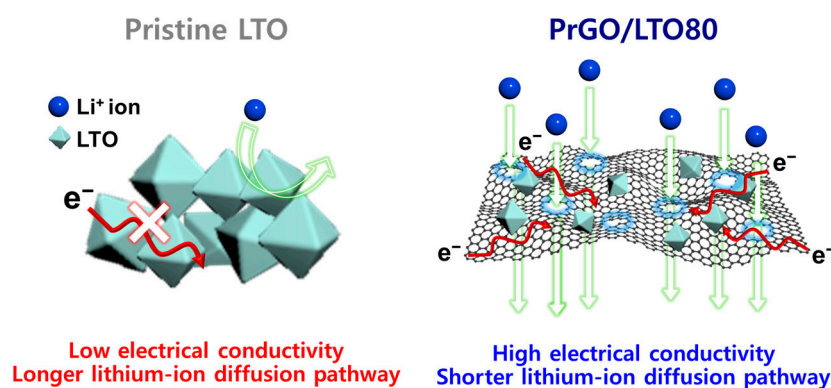


Figure 11. Plausible mechanism for attaining high electrical conductivity and a shorter lithium-ion diffusion property by adding PrGO to pristine LTO.

4. Conclusions

In this research, we successfully synthesized a novel plasma-reduced graphene oxide/lithium titanate oxide (PrGO/LTO) composite and demonstrated its effectiveness as an anode material for lithium-ion capacitors (LICs). The PrGO/LTO composite was prepared using an innovative approach that combined freeze-drying with plasma treatment, resulting in a unique porous three-dimensional (3D) structure. This structural design played a crucial role in enhancing the electrochemical performance of the material, particularly by improving lithium-ion diffusion and preventing the restacking of graphene oxide. Our analysis revealed that the PrGO/LTO composite with an 80% LTO mixing ratio (PrGO/LTO80) exhibited the most optimal performance. In half-cell tests, PrGO/LTO80 achieved a specific capacity of 73.0 mAh g^{-1} at 20 C, demonstrating an effective balance between energy and power densities. This optimal composition was further validated in full-cell LIC tests, where PrGO/LTO80 delivered an impressive energy density of 40.3 Wh kg^{-1} and a power density of 2000 W kg^{-1} . Additionally, the composite showed excellent cycle stability, retaining 94.1% of its capacitance after 2000 charge/discharge cycles, highlighting its potential for long-term applications.

The novelty of this work lies in the synthesis method, which integrates plasma-reduced graphene oxide with lithium titanate oxide in a way that enhances the intrinsic properties of both materials. The innovative freeze-drying process combined with plasma treatment not only addresses the common issues of low electrical conductivity and limited high-rate capability in traditional LTO anodes but also promotes the development of a high-performance anode with superior energy storage capabilities. This study not only advances the current understanding of LIC anode materials but also opens new pathways for designing next-generation energy storage systems. The PrGO/LTO composite, particularly in its

optimal configuration, presents a promising candidate for future high-energy-density LIC applications, offering both high efficiency and durability.

Supplementary Materials: The following supporting information can be downloaded at: <https://www.mdpi.com/article/10.3390/batteries10090311/s1>, Figure S1: SEM micrographs of (a) GO/LTO60, (b) GO/LTO70, (c) GO/LTO90, (d) PrGO/LTO60, (e) PrGO/LTO70, and (f) PrGO/LTO90 composites. Figure S2: XPS survey of (a) pristine LTO, (b) GO, (c) GO/LTO80, and (d) PrGO/LTO80. Figure S3: (a–c) XPS Li 1s and (d–f) Ti 2p spectra of pristine LTO, GO/LTO80, and PrGO/LTO80. Figure S4: XPS O 1s spectra of (a) pristine LTO, (b) GO, (c) GO/LTO80, and (d) PrGO/LTO80. Table S1: BET surface areas and pore volumes of pristine LTO, GO, GO/LTO, and PrGO/LTO. Figure S5: Charge/discharge curves of pristine LTO/Li half-cell at various C-rates. Table S2: Specific capacities of PrGO/LTO-based electrode at various C-rates. Figure S6: (a) GCD curves of activated carbon/Li half-cell at various current densities. (b) Specific capacitances of activated carbon/Li half-cell calculated from the GCD curves.

Author Contributions: C.-G.K. and S.J.: Conceptualization, Formal Analysis, Investigation, Validation, Data Curation, Writing—Original Draft, Writing—Review and Editing; Z.O.: Investigation, Validation, Data Curation, Writing—Original Draft; J.K.: Investigation, Validation, Writing—Review and Editing; Y.-H.R.: Visualization, Validation, Data Curation; J.N.: Validation, Writing—Review and Editing; W.-C.O.: Investigation, Supervision; C.-M.Y.: Conceptualization, Formal Analysis, Investigation, Validation, Visualization, Methodology, Data Curation, Writing—Original Draft, Writing—Review and Editing, Supervision, Project Administration, Funding Acquisition. All authors have read and agreed to the published version of the manuscript.

Funding: This research was supported by the development of a high-power supercapacitor R&D program of MOTIE/KEIT [00156073, Development of lithium-ion capacitors for the control of load variation of hydrogen vehicles, 2024].

Data Availability Statement: Data are contained within the article.

Conflicts of Interest: The authors declare no conflicts of interest.

References

1. Peng, J.; Meng, J.; Chen, D.; Liu, H.; Hao, S.; Sui, X.; Du, X. A Review of Lithium-Ion Battery Capacity Estimation Methods for Onboard Battery Management Systems: Recent Progress and Perspectives. *Batteries* **2022**, *8*, 229. [CrossRef]
2. Pameté, E.; Köps, L.; Kreth, F.A.; Pohlmann, S.; Varzi, A.; Brousse, T.; Balducci, A.; Presser, V. The Many Deaths of Supercapacitors: Degradation, Aging, and Performance Fading. *Adv. Energy Mater.* **2023**, *13*, 2301008. [CrossRef]
3. Pandey, D.; Kumar, K.S.; Thomas, J. Supercapacitor electrode energetics and mechanism of operation: Uncovering the voltage window. *Prog. Mater. Sci.* **2024**, *141*, 101219. [CrossRef]
4. Guo, L.; Hu, P.; Wei, H. Development of supercapacitor hybrid electric vehicle. *J. Energy Storage* **2023**, *65*, 107269. [CrossRef]
5. Oyedotun, K.O.; Ighalo, J.O.; Amaku, J.F.; Olisah, C.; Adeola, A.O.; Iwuozor, K.O.; Akpomie, K.G.; Conradie, J.; Adegoke, K.A. Advances in Supercapacitor Development: Materials, Processes, and Applications. *J. Electron. Mater.* **2023**, *52*, 96–129. [CrossRef]
6. Olabi, A.G.; Abbas, Q.; Al Makky, A.; Abdelkareem, M.A. Supercapacitors as next generation energy storage devices: Properties and applications. *Energy* **2022**, *248*, 123617. [CrossRef]
7. Hung, P.Y.; Zhang, H.; Lin, H.; Guo, Q.; Lau, K.T.; Jia, B. Specializing liquid electrolytes and carbon-based materials in EDLCs for low-temperature applications. *J. Energy Chem.* **2022**, *68*, 580–602. [CrossRef]
8. Zou, K.; Cai, P.; Cao, X.; Zou, G.; Hou, H.; Ji, X. Carbon materials for high-performance lithium-ion capacitor. *Curr. Opin. Electrochem.* **2020**, *21*, 31–39. [CrossRef]
9. Dong, S.; Lv, N.; Wu, Y.; Zhu, G.; Dong, X. Lithium-ion and sodium-ion hybrid capacitors: From insertion-type materials design to devices construction. *Adv. Funct. Mater.* **2021**, *31*, 2100455. [CrossRef]
10. Sun, C.; Zhang, X.; Li, C.; Wang, K.; Sun, X.; Ma, Y. High-efficiency sacrificial prelithiation of lithium-ion capacitors with superior energy-storage performance. *Energy Storage Mater.* **2020**, *24*, 160–166. [CrossRef]
11. Lee, H.G.; Kim, S.Y.; Lee, J.S. Dynamic observation of dendrite growth on lithium metal anode during battery charging/discharging cycles. *Npj Comput. Mater.* **2022**, *8*, 103. [CrossRef]
12. Jin, L.; Guo, X.; Shen, C.; Qin, N.; Zheng, J.; Wu, Q.; Zhang, C.; Zheng, J.P. A universal matching approach for high power-density and high cycling-stability lithium ion capacitor. *J. Power Sources* **2019**, *441*, 227211. [CrossRef]
13. Xu, G.; Han, P.; Dong, S.; Liu, H.; Cui, G.; Chen, L. $\text{Li}_4\text{Ti}_5\text{O}_{12}$ -based energy conversion and storage systems: Status and prospects. *Coord. Chem. Rev.* **2017**, *343*, 139–184. [CrossRef]
14. Shi, X.; Yu, S.; Deng, T.; Zhang, W.; Weitao, Z. Unlock the potential of $\text{Li}_4\text{Ti}_5\text{O}_{12}$ for high-voltage/long-cycling-life and high-safety batteries: Dual-ion architecture superior to lithium-ion storage. *J. Energy Chem.* **2020**, *44*, 13–18. [CrossRef]

15. Llaín-Jiménez, H.A.; Buchberger, D.A.; Winkowska-Struzik, M.; Ratyński, M.; Krajewski, M.; Boczar, M.; Hamankiewicz, B.; Czerwiński, A. Correlation between Lithium Titanium Oxide Powder Morphology and High Rate Performance in Lithium-Ion Batteries. *Batteries* **2022**, *8*, 168. [[CrossRef](#)]
16. Tang, Y.; Huang, F.; Zhao, W.; Liu, Z.; Wan, D. Synthesis of graphene-supported $\text{Li}_4\text{Ti}_5\text{O}_{12}$ nanosheets for high rate battery application. *J. Mater. Chem.* **2012**, *22*, 11257–11260. [[CrossRef](#)]
17. Pawlitzek, F.; Althues, H.; Schumm, B.; Kaskel, S. Nanostructured Networks for Energy Storage: Vertically Aligned Carbon Nanotubes (VACNT) as Current Collectors for High-Power $\text{Li}_4\text{Ti}_5\text{O}_{12}$ (LTO)/ LiMn_2O_4 (LMO) Lithium-Ion Batteries. *Batteries* **2017**, *3*, 37. [[CrossRef](#)]
18. An, D.; Shen, L.; Lei, D.; Wang, L.; Ye, H.; Li, B.; Kang, F.; He, Y.-B. An ultrathin and continuous $\text{Li}_4\text{Ti}_5\text{O}_{12}$ coated carbon nanofiber interlayer for high rate lithium sulfur battery. *J. Energy Chem.* **2019**, *31*, 19–26. [[CrossRef](#)]
19. Lim, S.; Park, H.; Yamamoto, G.; Lee, C.; Suk, J.W. Measurements of the Electrical Conductivity of Monolayer Graphene Flakes Using Conductive Atomic Force Microscopy. *Nanomaterials* **2021**, *11*, 25785. [[CrossRef](#)]
20. Wang, X.; Shi, G. Flexible graphene devices related to energy conversion and storage. *Energy Environ. Sci.* **2015**, *8*, 790–823. [[CrossRef](#)]
21. Doñoro, Á.; Muñoz-Mauricio, Á.; Etacheri, V. High-Performance Lithium Sulfur Batteries Based on Multidimensional Graphene-CNT-Nanosulfur Hybrid Cathodes. *Batteries* **2021**, *7*, 26. [[CrossRef](#)]
22. Albers, P.W.; Leich, V.; Ramirez-Cuesta, A.J.; Cheng, Y.; Hönig, J.; Parker, S.F. The characterisation of commercial 2D carbons: Graphene, graphene oxide and reduced graphene oxide. *Mater. Adv.* **2022**, *3*, 2810–2826. [[CrossRef](#)]
23. Kim, J.; Kim, M.; Cho, S.; Yoon, C.-M.; Lee, C.; Ryu, J.; Jang, J. Multidimensional Polyaniline/Reduced Graphene Oxide/Silica Nanocomposite for Efficient Supercapacitor Electrodes. *ChemNanoMat* **2016**, *2*, 236–241. [[CrossRef](#)]
24. Bouzina, A.; Perrot, H.; Sel, O.; Debiemme-Chouvy, C. Preventing Graphene from Restacking *via* Bioinspired Chemical Inserts: Toward a Superior 2D Micro-supercapacitor Electrode. *ACS Appl. Nano Mater.* **2021**, *4*, 4964–4973. [[CrossRef](#)]
25. Cheng, J.-H.; Chen, Y.-H.; Yeh, Y.-S.; Hy, S.; Kuo, L.-Y.; Hwang, B.-J. Enhancement of Electrochemical Properties by Freeze-dried Graphene Oxide via Glucose-assisted Reduction. *Electrochim. Acta* **2016**, *197*, 146–151. [[CrossRef](#)]
26. Wang, C.; Chen, X.; Wang, B.; Huang, M.; Wang, B.; Jiang, Y.; Suof, R. Freeze-Casting Produces a Graphene Oxide Aerogel with a Radial and Centrosymmetric Structure. *ACS Nano* **2018**, *12*, 5816–5825. [[CrossRef](#)] [[PubMed](#)]
27. Liu, C.; Qiu, Y.; Liu, Y.; Xu, K.; Zhao, N.; Lao, C.; Shen, J.; Chen, Z. Novel 3D grid porous $\text{Li}_4\text{Ti}_5\text{O}_{12}$ thick electrodes fabricated by 3D printing for high performance lithium-ion batteries. *J. Adv. Ceram.* **2022**, *11*, 295–307. [[CrossRef](#)]
28. Ma, Y.; Chang, H.; Zhang, M.; Chen, Y. Graphene-Based Materials for Lithium-Ion Hybrid Supercapacitors. *Adv. Mater.* **2015**, *27*, 5296–5308. [[CrossRef](#)]
29. Tian, Y.; Yu, Z.; Cao, L.; Zhang, X.L.; Sun, C.; Wang, D.-W. Graphene oxide: An emerging electromaterial for energy storage and conversion. *J. Energy Chem.* **2021**, *55*, 323–344. [[CrossRef](#)]
30. Alazmi, A.; Tall, O.E.; Rasul, S.; Hedhili, M.N.; Patole, S.P.; Costa, P.M. A process to enhance the specific surface area and capacitance of hydrothermally reduced graphene oxide. *Nanoscale* **2016**, *8*, 17782–17787. [[CrossRef](#)]
31. Zhao, J.; Rafat, M.N.; Yoon, C.-M.; Oh, W.-C. Novel Approach to Synthesis of AgZnS and TiO_2 Decorated on Reduced Graphene Oxide Ternary Nanocomposite for Hydrogen Evolution Effect of Enhanced Synergetic Factors. *Nanomaterials* **2022**, *12*, 3639. [[CrossRef](#)] [[PubMed](#)]
32. Akada, K.; Obata, S.; Saiki, K. Radio-frequency plasma assisted reduction and nitrogen doping of graphene oxide. *Carbon* **2022**, *189*, 571–578. [[CrossRef](#)]
33. Wu, S.; Su, F.; Dong, X.; Ma, C.; Pang, L.; Peng, D.; Wang, M.; He, L.; Zhang, Z. Development of glucose biosensors based on plasma polymerization-assisted nanocomposites of polyaniline, tin oxide, and three-dimensional reduced graphene oxide. *Appl. Surf. Sci.* **2017**, *401*, 262–270. [[CrossRef](#)]
34. Kondratowicz, I.; Nadolska, M.; Şahin, S.; Łapiński, M.; Przeźniak-Welenc, M.; Sawczak, M.; Yu, E.H.; Sadowski, W.; Żelechowska, K. Tailoring properties of reduced graphene oxide by oxygen plasma treatment. *Appl. Surf. Sci.* **2018**, *440*, 651–659. [[CrossRef](#)]
35. Shabin, M.; Hanaa, M.H.; Ranwen, O.; Shasha, L.; Hongyu, M.; Xiaofang, C.; Tam, S.; Huanting, W. Effect of oxygen plasma treatment on the nanofiltration performance of reduced graphene oxide/cellulose nanofiber composite membranes. *Green Chem. Eng.* **2021**, *2*, 122–131.
36. Jianlang, F.; Yunqing, Y.; Meng, X.; Ganbg, W.; Yu, K. Synthetic routes of the reduced graphene oxide. *Chem. Pap.* **2020**, *74*, 3767–3783.
37. Wang, S.; Wang, R.; Zhao, Q.; Ren, L.; Wen, J.; Chang, J.; Fang, X.; Hu, N.; Xu, C. Freeze-drying induced self-assembly approach for scalable constructing MoS_2 /graphene hybrid aerogels for lithium-ion batteries. *J. Colloid Interface Sci.* **2019**, *544*, 37–45. [[CrossRef](#)]
38. Noh, J.; Jekal, S.; Yoon, C.-M. Polyaniline-Coated Mesoporous Carbon Nanosheets with Fast Capacitive Energy Storage in Symmetric Supercapacitors. *Adv. Sci.* **2023**, *10*, 2301923. [[CrossRef](#)]
39. Yoon, C.-M.; Jekal, S.; Kim, D.-H.; Noh, J.; Kim, J.; Kim, H.-Y.; Kim, C.-G.; Chu, Y.-R.; Oh, W.-C. 3D Hierarchically Structured Tin Oxide and Iron Oxide-Embedded Carbon Nanofiber with Outermost Polypyrrole Layer for High-Performance Asymmetric Supercapacitor. *Nanomaterials* **2023**, *13*, 1614. [[CrossRef](#)]
40. Hummers, W.S.; Offeman, R.E. Preparation of Graphitic Oxide. *J. Am. Chem. Soc.* **1958**, *80*, 1339. [[CrossRef](#)]
41. Wang, G.; Wang, H.; Ma, G.; Du, X.; Du, L.; Jing, P.; Wang, Y.; Wu, K.; Wu, H.; Wang, Q.; et al. Investigation on process mechanism of a novel energy-saving synthesis for high performance $\text{Li}_4\text{Ti}_5\text{O}_{12}$ anode material. *J. Energy Chem.* **2022**, *70*, 266–275. [[CrossRef](#)]

42. Liyuan, Z.; Gang, H.; Dali, Z.; Jiabei, Z.; Qianqian, Y. Study on transformation mechanism of lithium titanate modified with hydrochloric acid. *Ionics* **2016**, *22*, 2007–2014.
43. Yoon, C.-M.; Jang, Y.; Noh, J.; Kim, J.; Lee, K.; Jang, J. Enhanced Electrorheological Performance of Mixed Silica Nanomaterial Geometry. *ACS Appl. Mater. Interface* **2017**, *9*, 36358–36367. [[CrossRef](#)] [[PubMed](#)]
44. Noh, J.; Hong, S.; Yoon, C.-M.; Lee, S.; Jang, J. Dual external field-responsive polyaniline-coated magnetite/silica nanoparticles for smart fluid applications. *Chem. Commun.* **2017**, *53*, 6645–6648. [[CrossRef](#)] [[PubMed](#)]
45. Lee, G.; Lee, C.; Yoon, C.-M.; Kim, M.; Jang, J. High-Performance Three-Dimensional Mesoporous Graphene Electrode for Supercapacitors using Lyophilization and Plasma Reduction. *ACS Appl. Mater. Interfaces* **2017**, *9*, 5222–5230. [[CrossRef](#)]
46. Hong, S.-A.; Lee, S.B.; Joo, O.-S.; Kang, J.W.; Cho, B.-W.; Lim, J.-S. Synthesis of lithium titanium oxide ($\text{Li}_4\text{Ti}_5\text{O}_{12}$) with ultrathin carbon layer using supercritical fluids for anode materials in lithium batteries. *J. Mater. Sci.* **2016**, *51*, 6220–6534. [[CrossRef](#)]
47. Gul, W.; Alrobei, H. Effect of Graphene Oxide Nanoparticles on the Physical and Mechanical Properties of Medium Density Fiberboard. *Polymers* **2021**, *13*, 1818. [[CrossRef](#)]
48. Dhaiveegan, P.; Peng, H.-T.; Michalska, M.; Xiao, Y.; Lin, H.-Y.; Hsieh, C.-K. Investigation of carbon coating approach on electrochemical performance of $\text{Li}_4\text{Ti}_5\text{O}_{12}/\text{C}$ composite anodes for high-rate lithium-ion batteries. *J. Solid State Electrochem.* **2018**, *22*, 1851–1861. [[CrossRef](#)]
49. Nikiforov, A.A.; Kuznetsov, D.K.; Nasara, R.N.; Govindarajan, K.; Lin, S.-K.; Pelegov, D.V. Fast and Slow Laser-Stimulated Degradation of Mn-Doped $\text{Li}_4\text{Ti}_5\text{O}_{12}$. *Batteries* **2022**, *8*, 251. [[CrossRef](#)]
50. Wunderlich, P.; Küpper, J.; Simon, U. Optimizing Discharge Capacity of Graphite Nanosheet Electrodes for Lithium–Oxygen Batteries. *Batteries* **2020**, *6*, 36. [[CrossRef](#)]
51. Shen, Y.; Jing, T.; Ren, W.; Zhang, J.; Jiang, Z.-G.; Yu, Z.-Z.; Dasari, A. Chemical and thermal reduction of graphene oxide and its electrically conductive polylactic acid nanocomposites. *Compos. Sci. Technol.* **2012**, *72*, 1430–1435. [[CrossRef](#)]
52. Babu, B.V.; Babu, K.V.; Aregai, G.T.; Devi, L.S.; Latha, B.M.; Reddi, M.S.; Samatha, K.; Veeraiyah, V. Structural and electrical properties of $\text{Li}_4\text{Ti}_5\text{O}_{12}$ anode material for lithium-ion batteries. *Results Phys.* **2018**, *9*, 284–289. [[CrossRef](#)]
53. Storm, M.M.; Overgaard, M.; Younesi, R.; Reeler, N.E.A.; Vosch, T.; Nielsen, U.G.; Edström, K.; Norby, P. Reduced graphene oxide for Li–air batteries: The effect of oxidation time and reduction conditions for graphene oxide. *Carbon* **2015**, *85*, 233–244. [[CrossRef](#)]
54. Qiao, X.; Liao, S.; You, C.; Chen, R. Phosphorus and Nitrogen Dual Doped and Simultaneously Reduced Graphene Oxide with High Surface Area as Efficient Metal-Free Electrocatalyst for Oxygen Reduction. *Catalysts* **2015**, *5*, 981–991. [[CrossRef](#)]
55. Su, H.; Zhang, C.; Li, X.; Wu, L.; Chen, Y. Aggregation prevention: Reduction of graphene oxide in mixed medium of alkylphenol polyoxyethylene (7) ether and 2-methoxyethanol. *RSC Adv.* **2018**, *8*, 39140–39148. [[CrossRef](#)] [[PubMed](#)]
56. Huang, Q.; Yang, Z.; Mao, J. Mechanisms of the decrease in low-temperature electrochemical performance of $\text{Li}_4\text{Ti}_5\text{O}_{12}$ -based anode materials. *Sci. Rep.* **2017**, *7*, 15292. [[CrossRef](#)]
57. Patat, S.; Rahman, S.; Dokan, F.K. The effect of sodium and niobium co-doping on electrochemical performance of $\text{Li}_4\text{Ti}_5\text{O}_{12}$ as anode material for lithium-ion batteries. *Ionics* **2022**, *28*, 3177–3185. [[CrossRef](#)]
58. Julien, C.M.; Mauger, A. Fabrication of $\text{Li}_4\text{Ti}_5\text{O}_{12}$ (LTO) as Anode Material for Li-Ion Batteries. *Micromachines* **2024**, *15*, 310. [[CrossRef](#)]
59. Shi, Y.; Wen, L.; Li, F.; Cheng, H.-M. Nanosized $\text{Li}_4\text{Ti}_5\text{O}_{12}$ /graphene hybrid materials with low polarization for high rate lithium ion batteries. *J. Power Sources* **2011**, *196*, 8610–8617. [[CrossRef](#)]
60. Xu, H.; Chen, J.; Li, Y.; Guo, X.; Shen, Y.; Wang, D.; Zhang, Y.; Wang, Z. Fabrication of $\text{Li}_4\text{Ti}_5\text{O}_{12}$ - TiO_2 Nanosheets with Structural Defects as High-Rate and Long-Life Anodes for Lithium-Ion Batteries. *Sci. Rep.* **2017**, *7*, 2960. [[CrossRef](#)]
61. Jekal, S.; Kim, J.; Kim, D.-H.; Noh, J.; Kim, M.-J.; Kim, H.-Y.; Kim, M.-S.; Oh, W.-C.; Yoon, C.-M. Synthesis of LiDAR-Detectable True Black Core/Shell Nanomaterial and Its Practical Use in LiDAR Applications. *Nanomaterials* **2022**, *12*, 3689. [[CrossRef](#)] [[PubMed](#)]
62. Jekal, S.; Otgonbayar, Z.; Noh, J.; Sa, M.; Kim, J.; Kim, C.-G.; Chu, Y.-R.; Kim, H.-Y.; Song, S.; Choi, H.; et al. Designing Novel LiDAR-Detectable Plate-Type Materials: Synthesis, Chemistry, and Practical Application for Autonomous Working Environment. *ACS Appl. Mater. Interfaces* **2024**, *16*, 19121–19136. [[CrossRef](#)] [[PubMed](#)]
63. Johra, F.T.; Jung, W.-G. Hydrothermally reduced graphene oxide as a supercapacitor. *Appl. Surf. Sci.* **2015**, *357*, 1911–1914. [[CrossRef](#)]
64. Díez, N.; Śliwak, A.; Gryglewicz, S.; Grzyb, B.; Gryglewicz, G. Enhanced reduction of graphene oxide by high-pressure hydrothermal treatment. *RSC Adv.* **2015**, *5*, 81831–81837. [[CrossRef](#)]
65. Coelho, J.; Pokel, A.; Park, S.-H.; McEvoy, N.; Berner, N.C.; Duesberg, G.S.; Nicolosi, V. Lithium Titanate/Carbon Nanotubes Composites Processed by Ultrasound Irradiation as Anodes for Lithium Ion Batteries. *Nature* **2017**, *7*, 7614. [[CrossRef](#)]
66. Gao, F.; Zhang, L.; Yang, L.; Zhou, X.; Zhang, Y. Structural Properties of Graphene Oxide Prepared from Graphite by Three Different Methods and the Effect on Removal of Cr(VI) from Aqueous Solution. *Nanomaterials* **2023**, *13*, 279. [[CrossRef](#)]
67. Anthony, G.; Genwei, C.; Mark, R.; Kun, W.; Yizhi, X.; Zhe, Q. Accelerated Synthesis of Ordered Mesoporous Carbons Using Plasma. *ACS Omega* **2023**, *8*, 15781–15789.
68. Mihiri, Y.G.E.; Sahrooz, R.; Rusen, Z.; Renwu, Z.; Patrick, J.C.; Anthony, P.M.; Jennifer, M.; Kostya, K.O. Power-to-decarbonization: Mesoporous carbon-MgO nanohybrid derived from plasma-activated seawater salt-loaded biomass for efficient CO_2 capture. *J. CO₂ Util.* **2021**, *53*, 101711.

69. Alireza, B.S.; Eslam, G.S.; Mohammad, H.; Maryam, S. Synergistic catalytic degradation of ciprofloxacin using magnetic carbon nanomaterial/NiFe₂O₄ promoted cold atmospheric pressure plasma jet: Influence of charcoal, multi walled carbon nanotubes and walnut shell. *J. Taiwan Inst. Chem. Eng.* **2022**, *132*, 104131.
70. Madani, S.S.; Schaltz, E.; Kær, S.K. Thermal Characterizations of a Lithium Titanate Oxide-Based Lithium-Ion Battery Focused on Random and Periodic Charge-Discharge Pulses. *Appl. Syst. Innov.* **2021**, *4*, 24. [[CrossRef](#)]
71. Truptimayee, A.; Anil, D.P.; Soobhankar, P. High-Temperature Electrochemical Performance of Lithium Titanate (Li₄Ti₅O₁₂) Anode Material in Secondary Lithium-ion Batteries. *J. Energy Storage* **2023**, *67*, 107529.
72. Shilei, D.; Zelong, J.; Jing, G.; Hongliang, Z.; Jiajia, C.; Dongdong, W. Carbon-coated lithium titanate: Effect of carbon precursor addition processes on the electrochemical performance. *Front. Chem. Sci. Eng.* **2021**, *15*, 148–155.
73. Kumar, N.; Setshedi, K.; Masukume, M.; Suprakas, S.R. Facile scalable synthesis of graphene oxide and reduced graphene oxide: Comparative investigation of different reduction methods. *Carbon Lett.* **2022**, *32*, 1031–1046. [[CrossRef](#)]
74. Abdolhosseinzadeh, S.; Asgharzadeh, H.; Seop, K.H. Fast and fully-scalable synthesis of reduced graphene oxide. *Sci. Rep.* **2015**, *5*, 10160. [[CrossRef](#)]
75. Zhang, X.; Zhang, X.; Sun, X.; An, Y.; Song, S.; Li, C.; Wang, K.; Su, F.; Chen, C.-M.; Liu, F.; et al. Electrochemical impedance spectroscopy study of lithium-ion capacitors: Modeling and capacity fading mechanism. *J. Power Sources* **2021**, *488*, 229454. [[CrossRef](#)]
76. Pohjalainen, E.; Kallioinen, J.; Kallio, T. Comparative study of carbon free and carbon containing Li₄Ti₅O₁₂ electrodes. *J. Power Sources* **2015**, *279*, 481–486. [[CrossRef](#)]
77. Zhu, Z.; Cheng, F.; Chen, J. Investigation of effects of carbon coating on the electrochemical performance of Li₄Ti₅O₁₂/C nanocomposites. *J. Mater. Chem. A* **2013**, *1*, 9484–9490. [[CrossRef](#)]
78. Lee, B.-G.; Lee, S.-H. Application of hybrid supercapacitor using granule Li₄Ti₅O₁₂/activated carbon with variation of current density. *J. Power Sources* **2017**, *343*, 545–549. [[CrossRef](#)]
79. Dsoke, S.; Fuchs, B.; Gucciardi, E.; Wohlfahrt-Mehrens, M. The importance of the electrode mass ratio in a Li-ion capacitor based on activated carbon and Li₄Ti₅O₁₂. *J. Power Sources* **2015**, *282*, 385–393. [[CrossRef](#)]
80. Lu, C.; Wang, X.; Zhang, X.; Peng, H.; Zhang, Y.; Wang, G.; Wang, Z.; Cao, G.; Umirov, N.; Bakenov, Z. Effect of graphene nanosheets on electrochemical performance of Li₄Ti₅O₁₂ in lithium-ion capacitors. *Ceram. Int.* **2017**, *46*, 6554–6562. [[CrossRef](#)]
81. Fu, C.C.; Zhang, L.J.; Peng, J.H.; Wang, H.; Yan, H. Synthesis of Li₄Ti₅O₁₂-reduced graphene oxide composite and its application for hybrid supercapacitors. *Ionics* **2016**, *22*, 1829–1836. [[CrossRef](#)]
82. Qian, Y.; Cai, X.; Zhang, C.; Jiang, H.; Zhou, L.; Li, B. A free-standing Li₄Ti₅O₁₂/graphene foam composite as anode material for Li-ion hybrid supercapacitor. *Electrochim. Acta* **2017**, *258*, 1311–1319. [[CrossRef](#)]
83. Deng, S.; Li, J.; Sun, S.; Wang, H.; Liu, J.; Yan, H. Synthesis and electrochemical properties of Li₄Ti₅O₁₂ spheres and its application for hybrid supercapacitors. *Electrochim. Acta* **2014**, *146*, 37–43. [[CrossRef](#)]
84. Xue, R.; Yan, J.; Jiang, L.; Yi, B. Fabrication of lithium titanate/graphene composites with high rate capability as electrode materials for hybrid electrochemical supercapacitors. *Mater. Chem. Phys.* **2015**, *160*, 375–382. [[CrossRef](#)]
85. Lee, B.-G.; Lee, S.-H.; Ahn, H.-J.; Yoon, J.-R. High performance hybrid supercapacitors using granule Li₄Ti₅O₁₂/Carbon nanotube anode. *J. Alloy. Compd.* **2018**, *748*, 882–888. [[CrossRef](#)]
86. Fan, Q.; Yang, M.; Meng, Q.; Cao, B.; Yu, Y. Activated-Nitrogen-Doped Graphene-Based Aerogel Composites as Cathode Materials for High Energy Density Lithium-Ion Supercapacitor. *J. Electrochem. Soc.* **2016**, *163*, A1736–A1742. [[CrossRef](#)]
87. Ye, Z.; Zhong, F.; Chen, Y.; Zou, Z.; Jiang, C. Unique CNTs-chained Li₄Ti₅O₁₂ nanoparticles as excellent high rate anode materials for Li-ion capacitors. *Ceram. Int.* **2022**, *48*, 20237–20244. [[CrossRef](#)]
88. Zhou, J.; Fu, Y.; Zhang, T.A. Cost-Effective Production Route of Li₄Ti₅O₁₂ Resisting Unsettled Market and Subsequent Application in the Li-Ion Capacitor. *Small Struct.* **2024**, *5*, 2300377. [[CrossRef](#)]
89. Divya, M.L.; Lü, H.Y.; Lee, Y.S.; Aravindan, V. Pre-lithiated Li_{4+x}Ti₅O₁₂ (0 ≤ x ≤ 3) anodes towards building high-performance Li-ion capacitors. *Sustain. Energy Fuels* **2022**, *6*, 4884–4892. [[CrossRef](#)]
90. Lee, S.H. Smart Multi-Layer Architecture Electrodes for High Energy Density Lithium-Ion Capacitors. *Batter. Supercaps.* **2022**, *6*, e202200380. [[CrossRef](#)]

Disclaimer/Publisher’s Note: The statements, opinions and data contained in all publications are solely those of the individual author(s) and contributor(s) and not of MDPI and/or the editor(s). MDPI and/or the editor(s) disclaim responsibility for any injury to people or property resulting from any ideas, methods, instructions or products referred to in the content.